Journal of Magnetic Resonance **147,** 340–352 (2000)
doi:10.1006/jmre.2000.2209, available online at http://www.idealibrary.com on IDEAL®

Condition Number as a Measure of Noise Performance of Diffusion Tensor Data Acquisition Schemes with MRI

Stefan Skare,* Maj Hedehus,† Michael E. Moseley,† and Tie-Qiang Li‡

**Karolinska MR Center, Karolinska Institute, S-171 76 Stockholm, Sweden; †Lucas MRI/MRS Research Center, Stanford University, Stanford, California 94305; and ‡Department of Psychology, Princeton University, Princeton, New Jersey 08544-1010*

Received June 13, 2000; revised August 21, 2000

Diffusion tensor mapping with MRI can noninvasively track neural connectivity and has great potential for neural scientific research and clinical applications. For each diffusion tensor imaging (DTI) data acquisition scheme, the diffusion tensor is related to the measured apparent diffusion coefficients (ADC) by a transformation matrix. With theoretical analysis we demonstrate that the noise performance of a DTI scheme is dependent on the condition number of the transformation matrix. To test the theoretical framework, we compared the noise performances of different DTI schemes using Monte-Carlo computer simulations and experimental DTI measurements. Both the simulation and the experimental results confirmed that the noise performances of different DTI schemes are significantly correlated with the condition number of the associated transformation matrices. We therefore applied numerical algorithms to optimize a DTI scheme by minimizing the condition number, hence improving the robustness to experimental noise. In the determination of anisotropic diffusion tensors with different orientations, MRI data acquisitions using a single optimum *b* value based on the mean diffusivity can produce ADC maps with regional differences in noise level. This will give rise to rotational variances of eigenvalues and anisotropy when diffusion tensor mapping is performed using a DTI scheme with a limited number of diffusion-weighting gradient directions. To reduce this type of artifact, a DTI scheme with not only a small condition number but also a large number of evenly distributed diffusion-weighting gradients in 3D is preferable.

Key Words: **diffusion tensor imaging; optimization; noise; condition number.**

INTRODUCTION

Diffusion tensor imaging (DTI) is an exciting new technique (*1–5*) for the assessment of white matter structural integrity and connectivity. The diffusion of water molecules in brain tissue is significantly hindered by the presence of cell membranes, myelin sheaths surrounding axons, and other structures. This is particularly true in white matter tracts where diffusion parallel to axons and myelin bundles is three to five times faster than diffusion perpendicular to the axons, rendering *in vivo* water diffusion highly anisotropic. The diffusion tensor contains information about both the direction and the magnitude of restriction, and several quantitative and absolute measures can be determined and mapped, such as the mean apparent diffusion coefficient (mean ADC, trace/3) and the degree of anisotropy (e.g., fractional anisotropy, FA).

Diffusion tensor imaging has great potential as a tool for neurological research and clinical applications. Water proton diffusion anisotropy abnormalities have been reported in a variety of disorders: stroke (*6*), schizophrenia (*7, 8*), alcoholism (*9*), developmental dyslexia (*10*), and multiple sclerosis (*11, 12*), as well as in normal brain development in the newborn (*13, 14*). In addition, recent studies have demonstrated the capability to automatically track white matter tracts using the information contained in the direction of the principal diffusivity (*15–17*). However, a number of technical challenges remain in the optimization of diffusion tensor imaging. Constructing the diffusion tensor requires the acquisition of a series of diffusion-weighted images (DWIs) with diffusion sensitization along a set of six or more noncollinear gradient directions. We refer to such a set of diffusion-weighting gradients as a DTI scheme, and we will focus on the optimization and performance of different DTI schemes.

Processing of the DTI data entails three steps: (a) determination of six independent diffusion tensor elements in the laboratory frame from the DWIs; (b) evaluation of eigenvalues (λ_1, λ_2, λ_3) and eigenvectors of the diffusion tensor D; and (*3*) calculation of diffusion anisotropy indices defined in terms of rotationally invariant eigenvalues and eigenvectors. Since DWIs typically have low signal-to-noise ratio (SNR), it is essential to minimize the noise propagation from the initial data acquisition to the final step of the procedure in order to obtain accurate anisotropy indices. While the error propagations in each individual step of the DTI data processing have been studied extensively (*1, 5, 18–22*), the noise performance of different DTI schemes used for the data acquisition has not been systematically investigated. There is currently no quantitative and objective measure of noise sensitivity and robustness for DTI schemes.

A number of data acquisition strategies (*9, 15, 20, 23–31*) have been proposed based largely on a matter of convenience

1090-7807/00 $35.00

for the geometrical description of the gradient directions or in terms of gradient hardware efficiency, but their noise performance is not well characterized. The methods from the literature that we have investigated are as follows:

1. tetrahedral, which is based on the tetrahedral method suggested by Conturo *et al.* (*20*) and extended to six diffusion directions by addition of the *xy* and *xz* directions (Table 1, scheme 1). Strictly speaking, this gradient configuration is not tetrahedral but is termed such here for simplicity;
2. dual-gradient, which always applies gradients (*9, 30, 31*) along two of the scanner axes simultaneously (Table 1, scheme 5);
3. decahedral, which was suggested by Skare and Nordell (*27*) and is a combination of the tetrahedral and dual-gradient schemes (Table 1, scheme 3);
4. Jones' nonisotropic (*28*) gradient scheme (Table 1, scheme 4);
5. tetraorthogonal (*15*), which is a combination of the tetrahedral method and the three orthogonal axes (Table 1, scheme 12);
6. the method suggested by Papadakis *et al.* (*26*), based on minimization of an "index of the DTI scheme" that is suggested as a quantitative estimate of the independent diffusion directions (Table 1, scheme 9);
7. the icosahedron scheme suggested by Muthupallai *et al.* (*25*), in which a "figure of merit for sensitivity" based on the angles between the diffusion direction and fiber axis is described (Table 1, scheme 11);
8. and finally Jones6, Jones10, Jones20, and Jones30, which are variations of the DTI scheme suggested by Jones *et al.* (*24*) with increasing numbers of diffusion directions. Jones *et al.* applied the theory behind electrostatic repulsion forces to calculate "optimal" gradient configurations. Using a downhill simplex method (*32*), the optimal configuration of *N* rods with positive unit charges on each end (corresponding to the *N* diffusion directions) is determined by minimizing the sum of the force between every possible pair of charges (Table 1, scheme 6, 7, 8, 10).

Only the first five schemes mentioned above are intuitively understandable in terms of *x*, *y*, and *z*, but all schemes including two additional schemes developed for this study (described under Methods) are listed in Table 1.

In this study, the noise propagation characteristics of DTI schemes are analyzed using the fundamental Stejskal–Tanner equation (*33*) characterizing the MRI signal in diffusion-weighted imaging experiments. We demonstrate that the noise sensitivity of a DTI scheme is determined by the condition number of the transformation matrix relating the diffusion tensor elements to the measured ADC. For the first time, numerical algorithms based on minimization of the condition number are proposed to find new DTI schemes. The theoretical framework is tested by systematic comparison with noise performance of different DTI schemes using Monte-Carlo simulations and experimental MRI measurements. Both the simulation and the experimental results demonstrate that the noise performance of a DTI scheme is significantly correlated with the condition number of the associated transformation matrices.

In addition to the choice of gradient directions, the ratio of the number of images without (S_0) and with (S_b) diffusion gradients is of importance and has been a subject of discussion (*24, 34, 35*). For isotropic samples or measurements of a single ADC value (*34, 35*), a ratio of 1:3.6 appears to be optimal whereas a ratio of 1:5.6 was shown to be optimal for anisotropic samples by Jones *et al.* (*24*). In this study, we have focused on the effect of diffusion directions, and we have therefore chosen a ratio of 1:6, which is close to the optimal 1:5.6, for all DTI schemes in order to obtain a fair comparison between schemes.

THEORY

Transformation Matrix for a DTI Acquisition Scheme

For a pulsed gradient spin-echo MRI experiment with an appropriate pulse sequence designed to eliminate imaging gradient "cross-talk" effects (*36*), extending the Stejskal–Tanner (*33*) equation in three dimensions and accounting for diffusion anisotropy, the MRI signal intensity, S_i, observed experimentally is described as

$$S_i = S_0 \exp(-b\mathbf{g}_i^{\mathrm{T}} \cdot \mathbf{D} \cdot \mathbf{g}_i), \qquad [1]$$

where S_0 is the signal intensity in the absence of any diffusion-weighting gradient, $\mathbf{D}$ is the representation of the diffusion tensor in the laboratory frame,

$$\mathbf{D} = \begin{pmatrix} D_{xx} & D_{xy} & D_{xz} \\ D_{xy} & D_{yy} & D_{yz} \\ D_{xz} & D_{yz} & D_{zz} \end{pmatrix}, \qquad [2]$$

and $\mathbf{g}_i = (g_{ix}\ g_{iy}\ g_{iz})^{\mathrm{T}}$ is the unit column vector of the diffusion-weighting gradient specifying the gradient orientation in the laboratory frame. The scalar b value is a function of the magnitude and timing of the diffusion-weighting gradient. For example, a pair of rectangular diffusion-weighting gradient pulses with amplitude G, duration δ, and separation interval of Δ yields $b = \gamma^2\delta^2(\Delta - \delta/3)G^2$ (γ is the proton gyromagnetic ratio). Introducing the following six-dimensional vectors,

$$\mathbf{X} = (d_1\ d_2\ d_3\ d_4\ d_5\ d_6)^{\mathrm{T}} = (D_{xx}\ D_{yy}\ D_{zz}\ D_{xy}\ D_{xz}\ D_{yz})^{\mathrm{T}}, \qquad [3]$$

and

$$\alpha_i = (g_{ix}^2\ g_{iy}^2\ g_{iz}^2\ 2g_{ix}g_{iy}\ 2g_{ix}g_{iz}\ 2g_{iy}g_{iz})^{\mathrm{T}}, \qquad [4]$$

TABLE 1
A List of Diffusion Schemes Investigated in This Work

1. Tetrahedral			2. Cond6			3. Decahedral			4. Jones noniso		
0.000	0.000	0.000	0.000	0.000	0.000	0.000	0.000	0.000	0.000	0.000	0.000
0.577	0.577	0.577	0.755	0.260	0.602	0.000	0.000	0.000	1.000	0.000	0.000
−0.577	−0.577	0.577	−0.479	0.711	0.515	0.577	0.577	0.577	0.000	1.000	0.000
0.577	−0.577	−0.577	−0.394	−0.630	0.669	−0.577	−0.577	0.577	0.000	0.000	1.000
−0.577	0.577	−0.577	−0.616	0.262	0.743	0.577	−0.577	−0.577	0.707	0.707	0.000
0.707	0.707	0.000	0.558	−0.741	0.375	−0.577	0.577	−0.577	0.707	0.000	0.707
0.707	0.000	0.707	−0.954	−0.067	0.292	0.707	0.707	0.000	0.000	0.707	0.707
						0.707	0.000	0.707	0.577	0.577	0.577
						0.000	0.707	0.707			
						0.707	−0.707	0.000			
5. Dual gradient			6. Jones (N = 10)			0.707	0.000	−0.707			
0.000	0.000	0.000	0.000	0.000	0.000	0.000	0.707	−0.707			
0.707	0.707	0.000	0.000	0.000	0.000						
0.707	0.000	0.707	1.000	0.000	0.000						
0.000	0.707	0.707	0.678	0.735	0.000				8. Jones (N = 30)		
0.707	−0.707	0.000	−0.556	0.504	0.661	7. Jones (N = 20)			0.000	0.000	0.000
0.707	0.000	−0.707	0.672	−0.733	0.106	0.000	0.000	0.000	0.000	0.000	0.000
0.000	0.707	−0.707	−0.012	−0.801	0.598	0.000	0.000	0.000	0.000	0.000	0.000
			−0.680	−0.310	0.664	0.000	0.000	0.000	0.000	0.000	0.000
			−0.045	−0.011	0.999	1.000	0.000	0.000	0.000	0.000	0.000
			−0.024	0.966	0.257	0.336	0.942	0.000	1.000	0.000	0.000
9. Papadakis			0.458	0.521	0.721	−0.405	0.606	0.685	0.166	0.986	0.000
0.000	0.000	0.000	0.658	−0.250	0.710	0.825	−0.513	−0.236	−0.110	0.664	0.740
0.000	0.000	0.000				0.006	−0.363	0.932	0.901	−0.419	−0.110
0.755	0.260	0.602				−0.811	−0.287	0.510	−0.169	−0.601	0.781
0.024	−0.341	0.940				0.852	−0.320	0.414	−0.815	−0.386	0.433
0.212	0.849	0.485	10. Jones (N = 6)			−0.240	0.959	0.149	0.656	0.366	0.660
−0.479	0.711	0.515	0.000	0.000	0.000	0.835	0.272	0.478	0.582	0.800	0.143
−0.394	−0.630	0.669	1.000	0.000	0.000	0.009	−0.904	0.427	0.900	0.259	0.350
−0.616	0.261	0.743	0.446	0.895	0.000	−0.063	−0.812	−0.580	0.693	−0.698	0.178
0.558	−0.740	0.375	0.447	0.275	0.851	−0.269	−0.390	−0.881	0.357	−0.924	−0.140
−0.954	−0.067	0.292	0.448	−0.723	−0.525	−0.422	−0.624	0.658	0.543	−0.488	−0.683
0.862	−0.402	0.309	0.447	−0.724	0.526	−0.601	0.779	−0.177	−0.525	−0.396	0.753
0.230	0.207	0.951	−0.449	−0.277	0.850	−0.516	0.086	−0.852	−0.639	0.689	0.341
−0.788	−0.615	0.035				−0.790	−0.607	0.087	−0.330	−0.013	−0.944
−0.035	−0.990	0.139				0.729	−0.181	−0.661	−0.524	−0.783	0.335
						0.265	−0.096	−0.960	0.609	−0.065	−0.791
						−0.561	−0.701	−0.440	0.220	−0.233	−0.947
						−0.405	0.631	−0.662	−0.004	−0.910	−0.415
									−0.511	0.627	−0.589
									0.414	0.737	0.535
			12. Tetraortho						−0.679	0.139	−0.721
11. Muthupallai			0.000	0.000	0.000	13. DSM (N = 6)			0.884	−0.296	0.362
0.000	0.000	0.000	0.577	0.577	0.577	0.000	0.000	0.000	0.262	0.432	0.863
0.851	0.526	0.000	−0.577	−0.577	0.577	0.910	0.416	0.000	0.088	0.185	−0.979
0.000	0.851	0.526	0.577	−0.577	−0.577	0.000	0.910	0.416	0.294	−0.907	0.302
0.526	0.000	0.851	−0.577	0.577	−0.577	0.416	0.000	0.910	0.887	−0.089	−0.453
0.851	−0.526	0.000	1.000	0.000	0.000	0.910	−0.416	0.000	0.257	−0.443	0.859
0.000	0.851	−0.526	0.000	1.000	0.000	0.000	0.910	−0.416	0.086	0.867	−0.491
−0.526	0.000	0.851	0.000	0.000	1.000	−0.416	0.000	0.910	0.863	0.504	−0.025

Eq. [1] can be rewritten as

$$S_i = S_0 \exp(-b\alpha_i^{\mathrm{T}}\mathbf{X}) \quad \text{or} \quad \alpha_i^{\mathrm{T}}\mathbf{X} = \ln(S_0/S_i)/b = \mathrm{ADC}_i. \qquad [5]$$

In Eq. [5] a logarithmic transformation is performed on the measured signal and the noise distribution in ADC is not strictly Gaussian at low SNR (*36*, *37*). For the simulation study discussed below, Gaussian distributed noise was directly added to the complex signal intensity (*18*, *37*). In the theoretical analysis of noise propagation from ADC to **X**, no assumption is imposed for the noise distribution, and the

nonlinear transformation introduced in Eq. [5] should have no effect on the analytical results. To solve for **X**, at least six independent ADC_i measurements using noncollinear gradients are required. For measurements using a generalized DTI scheme with $N \geq 6$ different gradient directions, we can define a vector

$$\mathbf{ADC} = (ADC_1\ ADC_2 \cdots ADC_N)^T \quad [6]$$

and a $N \times 6$ matrix

$$\mathbf{A} = (\alpha_1\ \alpha_2 \cdots \alpha_N)^T. \quad [7]$$

We have

$$\mathbf{A}\ \mathbf{X} = \mathbf{ADC}. \quad [8]$$

Since each DTI scheme contains at least six noncollinear gradients, the rank of matrix **A** is equal to 6 and **X** can be uniquely determined. The matrix **A** is solely dependent on the directions of the diffusion-weighting gradients and is referred to as the transformation matrix for the corresponding DTI scheme.

Error Propagation from ADC Measurements to Tensor Elements

When $N > 6$, Eq. [8] is overdetermined and the pseudoinverse of the transformation matrix, $\mathbf{A}^{-1}$, can be computed using the singular value decomposition algorithm. If **X** is the exact solution corresponding to the exact **ADC** values and **X′** is the calculated solution from Eq. [8] corresponding to the measured **ADC′** values with experimental errors, the errors for **X** and **ADC** are $\Delta\mathbf{X} = \|\mathbf{X} - \mathbf{X}'\|$ and $\Delta\mathbf{ADC} = \|\mathbf{ADC} - \mathbf{ADC}'\|$, respectively. If $\|\cdot\|$ represents the norm of a vector or matrix (*38*), we have

$$\Delta\mathbf{X} = \mathbf{A}^{-1}\Delta\mathbf{ADC},\ \|\Delta\mathbf{X}\| \leq \|\mathbf{A}^{-1}\|\|\Delta\mathbf{ADC}\| \quad [9]$$

$$\mathbf{A}\Delta\mathbf{X} = \Delta\mathbf{ADC},\ \frac{\|\Delta\mathbf{ADC}\|}{\|\mathbf{A}\|} \leq \|\Delta\mathbf{X}\|. \quad [10]$$

Therefore,

$$\frac{\|\Delta\mathbf{ADC}\|}{\|\mathbf{A}\|} \leq \|\Delta\mathbf{X}\| \leq \|\mathbf{A}^{-1}\|\|\Delta\mathbf{ADC}\|. \quad [11]$$

By the same reasoning used to derive Eq. [11], we have

$$\frac{\|\mathbf{ADC}\|}{\|\mathbf{A}\|} \leq \|\mathbf{X}\| \leq \|\mathbf{A}^{-1}\|\|\mathbf{ADC}\|. \quad [12]$$

It follows from Eqs. [11] and [12] that

$$\frac{1}{\|\mathbf{A}\|\|\mathbf{A}^{-1}\|}\frac{\|\Delta\mathbf{ADC}\|}{\|\mathbf{ADC}\|} \leq \frac{\|\Delta\mathbf{X}\|}{\|\mathbf{X}\|} \leq \|\mathbf{A}\|\|\mathbf{A}^{-1}\|\frac{\|\Delta\mathbf{ADC}\|}{\|\mathbf{ADC}\|}. \quad [13]$$

The scalar quantity $\|A\|\|A^{-1}\|$ is called the condition number of matrix **A** (*38*) and is denoted by cond(**A**). Thus

$$\frac{1}{\text{cond}(\mathbf{A})}\frac{\|\Delta\mathbf{ADC}\|}{\|\mathbf{ADC}\|} \leq \frac{\|\Delta\mathbf{X}\|}{\|\mathbf{X}\|} \leq \text{cond}(\mathbf{A})\frac{\|\Delta\mathbf{ADC}\|}{\|\mathbf{ADC}\|}. \quad [14]$$

This expression relates the relative error in the diffusion tensor elements, $\epsilon_x = \|\Delta\mathbf{X}\|/\|\mathbf{X}\|$, to the relative error in the ADC measurements, $\epsilon_{ADC} = \|\Delta\mathbf{ADC}\|/\|\mathbf{ADC}\|$. If the condition number is close to 1, ϵ_x will be close to ϵ_{ADC}. If the condition number is large, the relative error in the estimated diffusion tensor elements could be several times larger than the experimental errors in **ADC**. Thus, cond(**A**) depends only on the directions of diffusion-weighting gradients and can be used a quantitative and objective measure of noise performance for a given DTI scheme. For isotropic diffusion, the experimental error, ϵ_{ADC}, is the same at a given *b* value irrespective of the directions of the applied diffusion-weighting gradients. For anisotropic diffusion, ϵ_{ADC} is likely to vary with the directions of the applied diffusion-weighting gradients, if we use the same *b* value optimized on the basis of the mean ADC as normally practiced. Not only the condition number of the transformation matrix but also the variations of ϵ_{ADC} must be taken into consideration in the minimization of ϵ_x. This point will be further discussed below.

METHODS

Algorithm to Find New DTI Schemes with Lower Condition Numbers

Using the condition number of the transformation matrix as a measure of noise performance, we developed a numerical algorithm to search for new DTI schemes with lower condition numbers. The essential part of the algorithm consists of a downhill simplex minimization procedure (*32*) to search for orientation angles that reduce the condition number. The algorithm is initiated by (a) *N* noncollinear gradient vectors of the same length in 3D spherical coordinates using *N* azimuth and elevation angle pairs (i.e., $2N$ dimensions) and (b) a simplex of $2N + 1$ dimensions of a certain size. The transformation matrix and its corresponding condition number were then calculated according to their definitions. The iteration was stopped when reductions in the conditional number were less than 10^{-12} or when the number of minimization cycles exceeded 50,000. The latter termination criteria never did occur. Two thousand different initial simplex sizes and different initial gradient vector sets were used, all resulting in the same

TABLE 2
A List of Investigated DTI Schemes and the Condition Numbers of Associated Transformation Matrices

Scheme number	Scheme name	Literature reference	Condition number
1	Tetrahedral	(*20*)	9.1479
2	Cond6	(*29*)	5.9888
3	Decahedral	(*27*)	2.7487
4	Jones noniso	(*28*)	2.5616
5	Dual-gradient	(*9, 30, 31*)	2.0000
6	Jones10	(*23, 24*)	1.6242
7	Jones20	(*23, 24*)	1.6152
8	Jones30	(*23, 24*)	1.5945
9	Papadakis	(*26*)	1.5872
10	Jones6	(*24*)	1.5826
11	Muthupallai	(*25*)	1.5811
12	Tetraortho	(*15*)	1.5275
13	DSM	(*29*)	1.3228

optimized condition number. Optimization was performed for $N = 6$, 10, 20, 30, and 40.

The minimization algorithm was computationally intensive. To improve efficiency the algorithm was implemented in C using routines from *Numerical Recipes in C* (*39*) rather than using the built-in optimization toolbox in MATLAB (The MathWorks, Inc.). The computations were performed on an Ultra Enterprise 250 server (Sun Microsystems, Mountain View, CA). The schemes that were found by this downhill simplex minimization are referred to as DSM schemes.

Monte-Carlo Simulations of DTI Schemes

In order to verify the theoretical relationship between the noise performance and condition number of the transformation matrix (Eq. [14]), 13 different DTI schemes were investigated by Monte-Carlo simulations for different degrees of diffusion anisotropy and tensor orientations. Besides the DTI schemes found in the literature (*9, 15, 20, 23–31*), the optimized DSM schemes discussed above and another artificially constructed scheme (referred to as cond6) with condition number 6 were included in the simulations to cover a wide range of condition numbers. The gradient configuration, condition number, and literature references for each DTI scheme are listed in Tables 1 and 2, sorted according to descending condition number. As shown in Table 2, most of the schemes have relatively small condition numbers whereas the tetrahedral scheme (scheme 1) has the highest condition number.

In all simulations, a "rice-shaped" diffusion tensor ellipsoid was assumed such that the tensor possessed axial symmetry ($\lambda_1 \geq \lambda_2 = \lambda_3$). Four different degrees of anisotropy with ratios of $\lambda_1/\lambda_2 = 1$, 1.25, 4, and 10 were studied, while keeping $\lambda_2/\lambda_3 = 1$. The average eigenvalue $\bar{\lambda} = (\lambda_1 + \lambda_2 + \lambda_3)/3$ was set equal to 1.0×10^{-9} m^2/s for all simulations, a value comparable to the mean ADC in normal brain parenchyma (*18, 31, 40, 41*). Orientations of the simulated diffusion tensor were evenly distributed in the entire 3D space by systematically varying the azimuth ($-180° \leq \theta \leq 180°$) and elevation ($0° \leq \phi \leq 90°$) angles for the principal diffusion tensor directions. Two hundred different orientations were simulated for each degree of diffusion anisotropy.

Each simulation involved the recalculation of the eigenvalues and eigenvectors of a predefined diffusion tensor after introducing experimental random noise in the diffusion-weighted images. The random noise was assumed to be Gaussian distributed with a standard deviation $\sigma = 1/\mathrm{SNR}$. We used $\mathrm{SNR} = 15$ for all simulations, which corresponds to a typical experimental value.

For each degree of anisotropy and orientation the following procedures were performed: (i) The diffusion tensor representation, D, in the laboratory frame was calculated using the predefined diffusion anisotropy and tensor orientation angles. (ii) ADC_i values along each gradient direction defined by a particular DTI scheme were determined from the diffusion tensor (D) and the transformation matrix (A) associated with the scheme according to Eq. [8]. (iii) DWI signal intensities, S_0 and S_b, were computed from the known ADC_i and b values ($b = 0$ and 900 s/mm^2). (iv) Gaussian-distributed random noise was added to the complex MRI signals. (v) Noise-perturbed signal intensities were used to recalculate the noise contaminated ADC values from which the diffusion tensor, its eigenvalues, and eigenvectors were recalculated. (vi) Fractional anisotropy was evaluated according to its definition,

$$\mathrm{FA} = \sqrt{\frac{3}{2}\frac{\sum_{i=1,2,3}(\lambda_i - \bar{\lambda})^2}{\sum_{i=1,2,3}\lambda_i^2}}, \qquad [15]$$

using the noise-perturbed eigenvalues of the diffusion tensor. The mathematical details of the above procedures are the same as those described previously (*18*). For each combination of anisotropy, orientation, and DTI scheme 10^4 repeated calculations were performed using MATLAB.

Statistical analysis of the simulation results included evaluation of the standard deviation of the fractional anisotropy (*1, 18*), $\sigma(\mathrm{FA})$, and bias of the fractional anisotropy, $\langle \Delta \mathrm{FA} \rangle$, according to

$$\sigma(\mathrm{FA}) = \sqrt{\frac{\sum_{i=1}^{M}\left(\mathrm{FA}_i - \frac{1}{M}\sum_{i=1}^{M}\mathrm{FA}_i\right)^2}{M-1}} \qquad [16]$$

$$\langle \Delta \mathrm{FA} \rangle = \frac{1}{M}\sum_{i=1}^{M}(\mathrm{FA}_i - \mathrm{FA}_{\mathrm{expected}}), \qquad [17]$$

where M is the number of repeated measurements using a given DTI scheme and FA_i is the fractional anisotropy value determined in each measurement. The bias is defined as the

difference in fractional anisotropy between the noise-free and noise-contaminated FA. The average standard deviation and bias over different degrees of diffusion anisotropy and orientation angles were calculated for each DTI scheme.

Phantom Study

MRI measurements were performed in a water phantom to verify the simulated and theoretical results. In order to eliminate motion artifacts and match the ADC of the phantom with the value of brain ADC, starch was added to the water resulting in an ADC of 1.2×10^{-3} mm^2/s. The MRI measurements were performed on a GE Signa 1.5-T (GE, Milwaukee, WI) whole-body MRI medical scanner equipped with Echo-Speed gradients using a diffusion-weighted spin-echo EPI (echo-planar imaging) sequence. Imaging parameters were TE/TR = 88/1000 ms, FOV = 200 mm, matrix size = 64 × 64, 3-mm slice thickness, and $b = 800$ s/mm^2.

Depending on the DTI scheme, a different number of diffusion-weighting gradients was applied simultaneously. Consequently, different minimum TE values can be achieved for different DTI schemes using the same b value. However, to facilitate the comparison between DTI schemes, T_2 weighting effects were kept constant across schemes by using the minimum TE that satisfied all schemes.

For diffusion schemes with more than six diffusion-weighting gradient directions, the data acquisition was longer and usually produced diffusion tensor measurements of higher accuracy due to an averaging effect. For quantitative comparison between the different DTI schemes, additional averaging was performed for schemes with a lower number of diffusion directions, so the total number of MRI measurements was approximately the same for all schemes. The ratio of acquisitions at $b = 0$ and $b = 800$ s/mm^2 was kept approximately at 1:6. Further details of data acquisition for each scheme are shown in Table 3.

The standard deviation in pixel j can be estimated from M repeated sessions according to Eq. [16]. Although the number of diffusion-weighting gradient directions is different for each DTI scheme (Table 3), about 140 images per scheme were collected. To avoid a long data acquisition time (especially important for the subsequent volunteer study) the experimental design outlined in Table 3 was only repeated twice ($M = 2$). To enhance the statistical power, the average value of σ_j(FA) over all pixels in an ROI covering the entire phantom on the imaged slice was calculated as

$$\langle \sigma(\mathrm{FA}) \rangle = \sum_{j=1}^{K} \sigma_j(\mathrm{FA})/K, \qquad [18]$$

where K is the number of pixels within the ROI. Here, an ROI in the center of the phantom containing $K \approx 1000$ pixels was chosen. Theoretically, the fractional anisotropy of the isotropic phantom is zero. Using $\mathrm{FA}_{\mathrm{expected}} = 0$ in Eq. [17], it is also possible to calculate the average bias, $\langle \Delta \mathrm{FA} \rangle$, for the phantom.

TABLE 3
MRI Data Acquisition Parameters Used for the Phantom and Human Studies

DTI scheme	Number of directions	S_0 measurements	Measurement averaging	Total No. of DWI measurements
1	6	1	20	140
2	6	1	20	140
3	10	2	12	144
4	7	1	18	144
5	6	1	20	140
6	10	2	12	144
7	20	3	6	138
8	30	5	4	140
9	10	2	12	144
10	6	1	20	140
11	6	1	20	140
12	7	1	18	144
13	6	1	20	140

Note. For each DTI scheme, about the same number of images (~140) were collected by adjusting the number of repeated measurements according to the number of diffusion-weighting gradient directions in each scheme.

Human Study

Finally, MRI measurements for each DTI scheme were performed in five healthy volunteers using the same sequence and MRI scanner described above. One axial slice through the corpus callosum was acquired for each subject. The DWI data acquisition parameters were TE = 95 ms, FOV = 240 mm, matrix size = 128 × 128, 4-mm slice thickness, and $b = 1000$ s/mm^2. As for the phantom, averaging was performed to keep the total number of images constant across schemes (Table 4).

To reduce respiratory artifacts, peripheral gating was used for the human study. The data were acquired using a fixed trigger delay of 400 ms after the R-peak and TR = 4 × RR. To reduce head motions between the repeated measurements the subjects were stabilized with foam padding fit tightly in the head coil. Eddy current effects in the diffusion-weighted images were corrected using the unwarping method described by de Crespigny and Moseley (*42*) prior to calculation of ADC maps.

As described for the phantom experiment, the experimental design detailed in Table 3 was repeatedly measured in two separate sessions from which the average standard deviation, $\langle \sigma(\mathrm{FA}) \rangle$, in an ROI encompassing the entire brain (within the slice) was calculated. This resulted in a total scan time of approximately 2 h for each subject. Both the diffusion tensor orientation and the degree of diffusion anisotropy at different locations of the brain are usually different. The spatially averaged standard deviation $\langle \sigma(\mathrm{FA}) \rangle$ described above reflects the average noise performance for each scheme over a wide range of diffusion anisotropy and tensor orientation.

TABLE 4
Diffusion Gradient Schemes Found by the Optimization of Condition Number Using the Downhill Simplex Method (DSM)

$N = 6$		
0.910	0.416	0.000
0.000	0.910	0.416
0.416	0.000	0.910
0.910	−0.416	0.000
0.000	0.910	−0.416
−0.416	0.000	0.910

$N = 10$		
0.997	0.047	−0.063
0.479	0.842	0.248
−0.299	0.549	0.780
0.716	−0.698	0.028
0.001	−0.864	0.504
−0.805	−0.230	0.547
−0.026	−0.191	0.981
−0.003	0.997	0.071
0.235	0.058	0.970
0.897	0.014	0.441

$N = 20$		
0.999	−0.013	0.044
0.139	0.989	0.048
−0.273	0.292	0.917
0.905	−0.421	−0.049
0.063	−0.201	0.977
−0.853	−0.268	0.449
0.959	−0.054	0.277
−0.241	0.961	0.137
0.875	0.217	0.433
−0.043	−0.923	0.382
−0.025	−0.897	−0.442
−0.224	−0.332	−0.916
−0.282	−0.639	0.716
−0.589	0.807	−0.043
−0.342	−0.047	−0.938
−0.858	−0.512	0.049
0.796	−0.205	−0.569
0.226	−0.060	−0.972
−0.342	−0.928	−0.151
−0.383	0.586	−0.714

$N = 30$		
0.995	0.079	0.068
0.029	0.995	0.097
−0.128	0.533	0.836
0.978	−0.196	0.068
−0.085	−0.632	0.770
−0.887	−0.255	0.385
0.541	0.486	0.687
0.443	0.889	0.121
0.971	0.203	0.125
0.459	−0.887	0.051
0.389	−0.912	−0.132
0.602	−0.510	−0.614
−0.287	−0.417	0.863
−0.807	0.566	0.166
−0.162	−0.209	−0.964
−0.328	−0.917	0.226
0.552	0.019	−0.834
0.320	−0.046	−0.946
−0.037	−0.982	−0.185
−0.657	0.293	−0.695
0.362	0.820	0.443
−0.686	0.164	−0.709
0.977	−0.171	0.129
−0.014	0.229	0.973
−0.110	0.260	−0.959
0.192	−0.921	0.340
0.988	0.053	−0.146
0.193	−0.077	0.978
0.005	0.961	−0.275
0.873	0.459	−0.166

$N = 40$		
0.995	0.078	0.068
0.030	0.995	0.096
−0.128	0.533	0.836
0.978	−0.196	0.067
−0.084	−0.633	0.770
−0.887	−0.256	0.385
0.542	0.486	0.685
0.442	0.889	0.121
0.971	0.203	0.124
0.459	−0.887	0.052
0.390	−0.911	−0.132
0.602	−0.511	−0.614
−0.288	−0.417	0.862
−0.807	0.566	0.168
−0.162	−0.208	−0.965
−0.328	−0.917	0.227
0.551	0.019	−0.834
0.320	−0.048	−0.946
−0.038	−0.982	−0.185
−0.657	0.291	−0.695
0.361	0.821	0.443
−0.685	0.162	−0.710
0.977	−0.171	0.130
−0.013	0.229	0.973
−0.108	0.260	−0.960
0.194	−0.920	0.340
0.988	0.053	−0.145
0.193	−0.079	0.978
0.005	0.962	−0.275
0.873	0.458	−0.167
0.997	0.048	−0.063
0.479	0.842	0.248
−0.299	0.549	0.780
0.716	−0.697	0.028
0.001	−0.863	0.505
−0.804	−0.230	0.548
−0.025	−0.190	0.981
−0.003	0.997	0.071
0.234	0.059	0.970
0.897	0.013	0.441

Note. The results are shown for five DSM schemes with number of diffusion encoding directions $N = 6$, 10, 20, 30, and 40.

It is important to realize that time and spatial averaging are only equivalent when the system is ergodic and the number of samples (K) is large. In our study, it was not practically feasible to do a large number of time samples (M) due to restraints on the total scan time per volunteer. We therefore rely on using a large number of samples. The number of pixels inside the brain available for spatial averaging was about 5000 (depending on the brain size), which was of the same order of magnitude as the number of repeated simulations performed in the time domain. Since the true fractional anisotropy in the brain is unknown *a priori*, it is impossible to make a reliable estimate of the measurement bias for each DTI scheme from the *in vivo* data.

RESULTS

Minimization of Condition Number

All DSM schemes ($N = 6$, 10, 20, 30, and 40) were typically obtained in less than 10 min. The condition number for the DSM schemes does not change with N but always reaches 1.3228, which is close to the ultimate theoretical min-

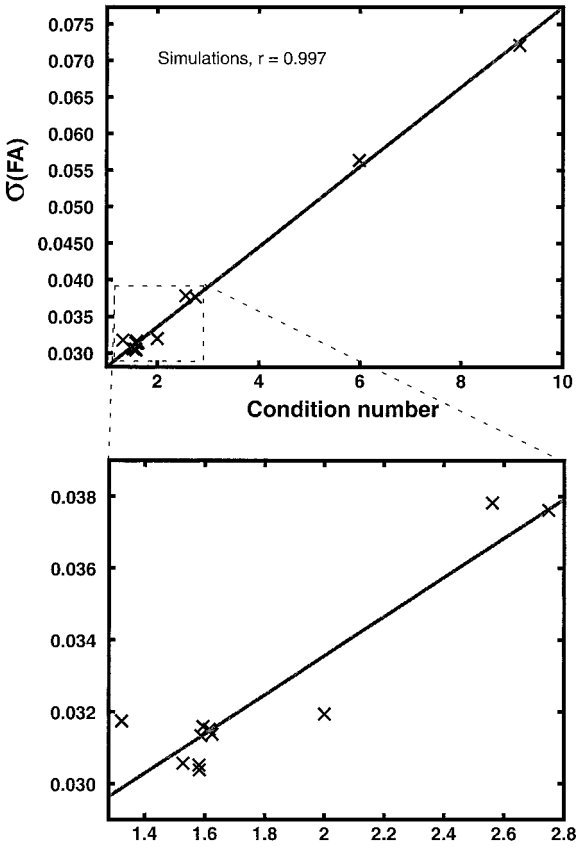

FIG. 1. Standard deviation of the fractional anisotropy, σ(FA), as a function of condition number. For each diffusion tensor imaging scheme, the simulation results averaged over four different degrees of diffusion anisotropy and 200 different tensor orientations are shown. The line denotes the linear regression analysis of σ(FA) against the condition number of the associated transformation matrix for each DTI scheme ($r = 0.997$ and $P < 0.001$). To better visualize the data for low condition numbers, the lower plot shows the data at another scale.

imum of 1. The gradient vectors are listed in Table 4 for each N. The gradient configuration for $N = 6$ is also detailed in Table 1 together with other schemes found in the literature.

Varying the starting scheme and the initial conditions had no impact on the final result when the iteration steps were sufficiently large. Furthermore, results from minimization with smaller N were always contained in the results with larger N.

Simulations

As expected from Eq. [14], the error propagation of a DTI scheme is highly correlated with the condition number of the associated transformation matrix ($r = 0.997$, $P < 0.001$) when all DWIs were acquired using the same b value. The transformation matrix for the tetrahedral scheme (*20*) has the largest condition number (9.1479) among the DTI schemes studied and the corresponding σ(FA) for the scheme is also the highest. This is demonstrated in Fig. 1, which shows σ(FA) as a function of condition numbers for different DTI schemes. The simulation results demonstrate significantly narrower error dispersion ranges for DTI data acquisition schemes with smaller condition numbers.

In addition to the propagation of experimental error, the noise-induced bias (*5*) is also an important characteristic for the performance of a DTI scheme. Similar to the standard deviation results, the bias of the fractional anisotropy is also significantly correlated with condition number. This is demonstrated for the isotropic case in Fig. 2a, which shows the average bias of the fractional anisotropy, $\langle\Delta\text{FA}\rangle$, as a function of condition number for the simulated data.

However, the standard deviation of the fractional anisotropy, σ(FA), depends significantly on the relative orientation between the diffusion-weighting gradient and the principal eigenvector of the diffusion tensor. This is illustrated in Fig. 3, which depicts the standard deviation of the fractional anisotropy as a function of azimuth and elevation angles of the principal tensor direction for three DTI schemes (Tetrahedral,

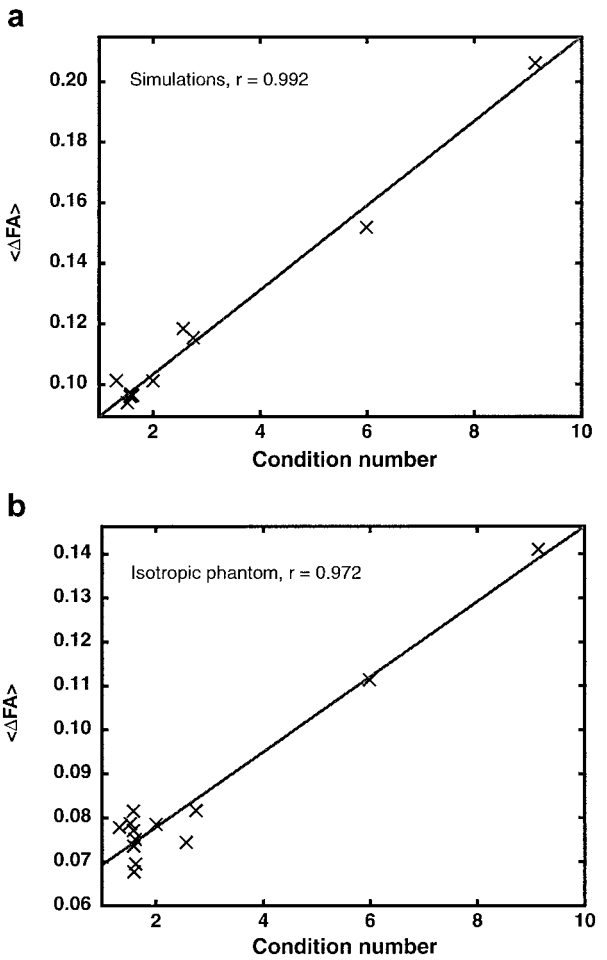

FIG. 2. The bias of the fractional anisotropy $\langle\Delta\text{FA}\rangle$ in the isotropic water phantom as a function of condition number. The results from Monte-Carlo computer simulations (a) and experimental MRI measurements (b) are shown. The lines denote the linear regression analysis of $\langle\Delta\text{FA}\rangle$ against the condition number of the associated transformation matrix for each DTI scheme.

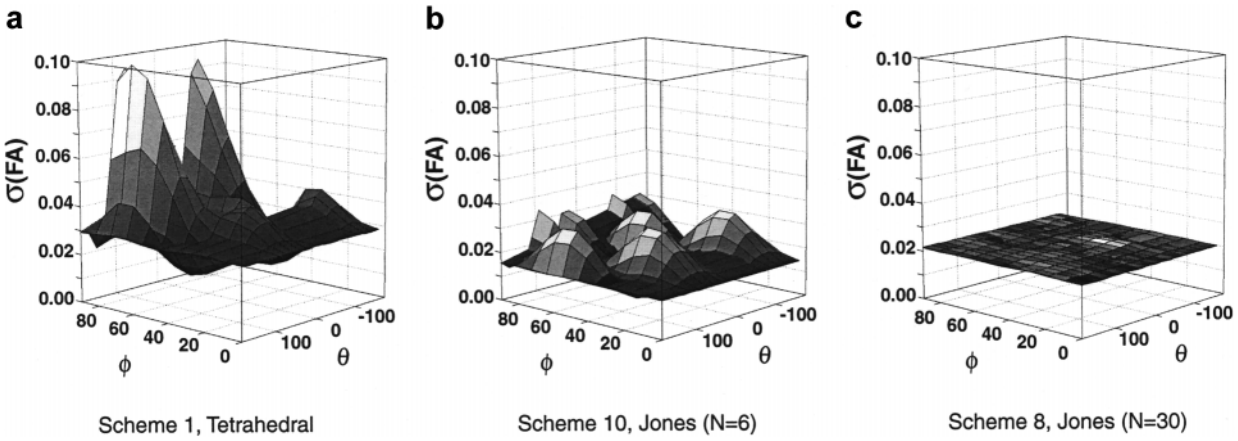

FIG. 3. Standard deviation of the fractional anisotropy, σ(FA), as a function of tensor orientation for three different DTI schemes. The tetrahedral scheme (a) has a substantially higher condition number. The Jones6 (b) and Jones30 (c) have similar condition numbers but a different number of diffusion-weighting gradient directions. FA gives a rotational invariant measure of diffusion anisotropy only when a DTI scheme with a low condition number and a large number of diffusion-weighting gradient directions is used.

Jones6, and Jones30). Comparing Figs. 3a and 3b, both differences in the average $\langle\sigma(\text{FA})\rangle$ and degree of rotational variance are clearly observable between the results for the tetrahedral and Jones6 schemes. Only the scheme Jones30 (Fig. 3c) produces low and rotational invariant σ(FA). Comparison of the DSM schemes with the Jones schemes with the same number (N) of diffusion-weighting directions reveals that the Jones schemes are still superior in terms of lowering noise and bias.

Phantom Study

The correlation between $\langle\sigma(\text{FA})\rangle$ and the condition number that was demonstrated using simulated results is also evident in the phantom data (Fig. 4). As the condition number is reduced from 9.15 for the tetrahedral scheme to 1.32 for the DSM scheme, the standard deviation of the fractional anisotropy was reduced by a factor of 2. These results agree well with the theoretical prediction that the condition number of the associated transformation matrix sets both the lower and the upper error limits for the diffusion tensor when the experimental noise level for ADC is constant.

The correlation of the average fractional anisotropy bias with the condition number is also verified in the phantom data, Fig. 2b. The results from simulations (Fig. 2a) and phantom measurements (Fig. 2b) are in good agreement, although the simulation results have a higher correlation coefficient (0.992 versus 0.972).

Human Study

Finally, data from the healthy volunteers show the same correlation between the average $\langle\sigma(\text{FA})\rangle$ and the condition number as the simulations and the phantom measurements, Fig. 5 ($r = 0.980$). The noise performance of different DTI schemes can also be qualitatively demonstrated by the quality of anisotropy maps measured using different schemes. Figure 6 shows a representative set of fractional anisotropy maps measured in a normal subject using four DTI schemes with significantly different condition numbers: tetrahedral (a), DSM (b), Jones6 (c), and Jones30 (d). Although the total number of DWI data acquisitions used for each scheme was nearly identical (see Table 3), the maps from the four schemes show clear differences in SNR, indicating that the robustness to noise propagation is very different for these schemes.

Compared with DTI schemes with condition numbers close to 1.5, the tetrahedral scheme has a high condition number of 9.148 and produces a much noisier fractional anisotropy map with poor resolution. Irrespective of the different degrees of anisotropy between regions of the main corpus callosum struc-

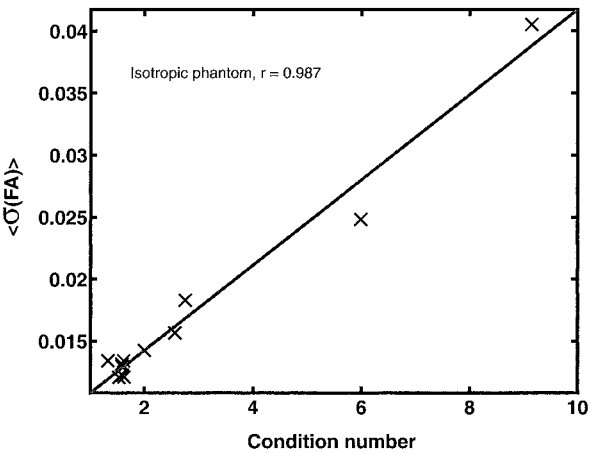

FIG. 4. The spatially averaged standard deviation of the fractional anisotropy, $\langle\sigma(\text{FA})\rangle$, versus condition number as measured in an isotropy water phantom using different DTI schemes. Results from an ROI in the center of the phantom containing approximately 1000 voxels are shown. The line shows the linear regression analysis of $\langle\sigma(\text{FA})\rangle$ against the condition number of the associated transformation matrix for each DTI scheme ($r = 0.987$ and $P < 0.001$).

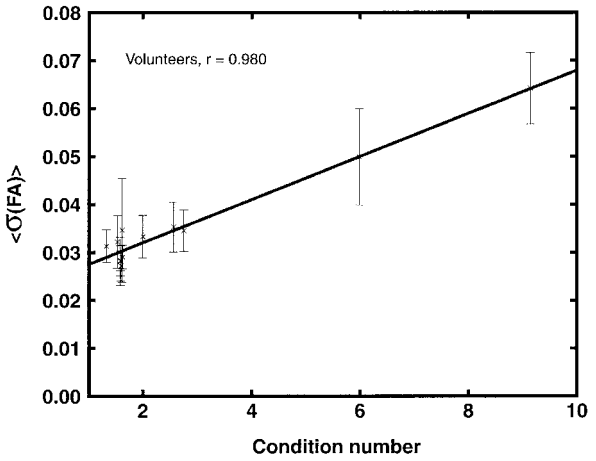

FIG. 5. The spatially averaged standard deviation of the fractional anisotropy, $\langle\sigma(\mathrm{FA})\rangle$, versus condition number as measured in five normal human subjects using different DTI schemes. The average result from all pixels inside the brain of the imaged slice is shown. The line denotes the linear regression analysis of $\langle\sigma(\mathrm{FA})\rangle$ against the condition number of the associated transformation matrix for each DTI scheme ($r = 0.980$ and $P < 0.001$).

tures and cortical gray matter, the entire map has a grainy appearance with discontinuous anisotropy variations.

In contrast, other FA maps showed clearly defined anisotropy structure with uniform and smooth anisotropy variations. Comparing results for schemes with similar condition numbers, the contrast between the strongly anisotropic white matter structures and low anisotropic cortical gray matter is further enhanced (Figs. 6b–6d) with the increased number of diffusion-weighting gradient directions.

DISCUSSION

In this study the noise performance of different DTI schemes was investigated by theoretical analysis and experimental validation. Assuming that all DWI acquisitions use a single optimal *b* value based on the mean diffusivity, the determination of the diffusion tensor is treated as a system of linear equations. The condition number of the transformation matrix, which is solely dependent on the orientations of the diffusion-weighting gradients, defines the lower and upper bounds of the error propagation from the experimental measurements to the estimated diffusion tensor parameters. We have identified the condition number of a DTI as an intuitive and objective measure of the noise performance for the DTI scheme. A comparison of different DTI schemes found in the literature using computer simulations and MRI experimental measurements has demonstrated that both the standard deviation and the bias of the estimated anisotropy are proportional to the condition number. Commonly used schemes (*9, 15, 20, 23–31*) differ significantly in noise performance because the associated transformation matrices have different condition numbers. In particular, the tetrahedral scheme with the highest condition number produces the noisiest anisotropy maps.

However, the condition number alone does not fully characterize the robustness of a DTI scheme. For isotropic diffusion, each ADC is expected to produce the same error irrespective of the direction of the diffusion-weighting gradients. For anisotropic diffusion, however, ADC measurements using the same *b* value will produce DWIs with SNR values depending on the relative orientation between the principal direction of the diffusion tensor and the diffusion-weighting gradient. Consequently, the errors in the calculated diffusion anisotropy not only are a function of the condition number but also are dependent on the relative orientation between the diffusion-weighting gradient and the principal eigenvector of the diffusion tensor. DTI schemes with a large number of uniformly distributed diffusion-weighting gradients can reduce this type of noise-induced rotational variance. Thus, for schemes with comparable condition number, the number of diffusion directions is also a critical factor. This is very clearly demonstrated by the comparison between Jones6 (Fig. 3b) and Jones30 (Fig. 3c) schemes. Although the two schemes have an almost identical condition number, the noise performance for varying orientations of the diffusion tensor is quite different. A unique of feature of the Jones schemes is that the diffusion-weighting gradients are always uniformly distributed in the entire 3D space irrespective of the total number of diffusion-weighting gradients used. Schemes with a low number of diffusion-weighting gradients cannot produce robust rotation invariant measurements of eigenvalues and anisotropy in the presence of experimental noise. Increasing the number of diffusion-weighting gradient directions as in the Jones30 scheme (*23*) greatly reduces σ(FA) and its dependence on the orientations of the diffusion ellipsoid.

For the first time, we show that a numerical algorithm can be used to optimize DTI schemes based on minimization of the condition number of the transformation matrix. This has the advantage of high reliability and efficiency in the design of DTI experiment. At present, DTI schemes with a condition number as low as 1.3228 were found and the schemes demonstrate good noise behavior compared to other DTI schemes with low condition numbers. The downhill simplex algorithm itself does not guarantee that the complex *N*-dimensional minimization process will encounter a global minimum (*32, 39*), but a few aspects of the minimization result indicate that our result is probably a global minimum: (1) The condition number of 1.3228 is close to the ultimate theoretical minimum of 1.0. (2) Restarting the minimization routine using the claimed minimum vertices does not produce different results. (3) The results from lower dimensional minimization with smaller *N* is always contained in the results with larger *N*. (4) The condition number does not change with *N*. Using the minimization of the condition number as a theoretical guide, the necessary condition of robustness to experimental noise can be guaranteed for the scheme.

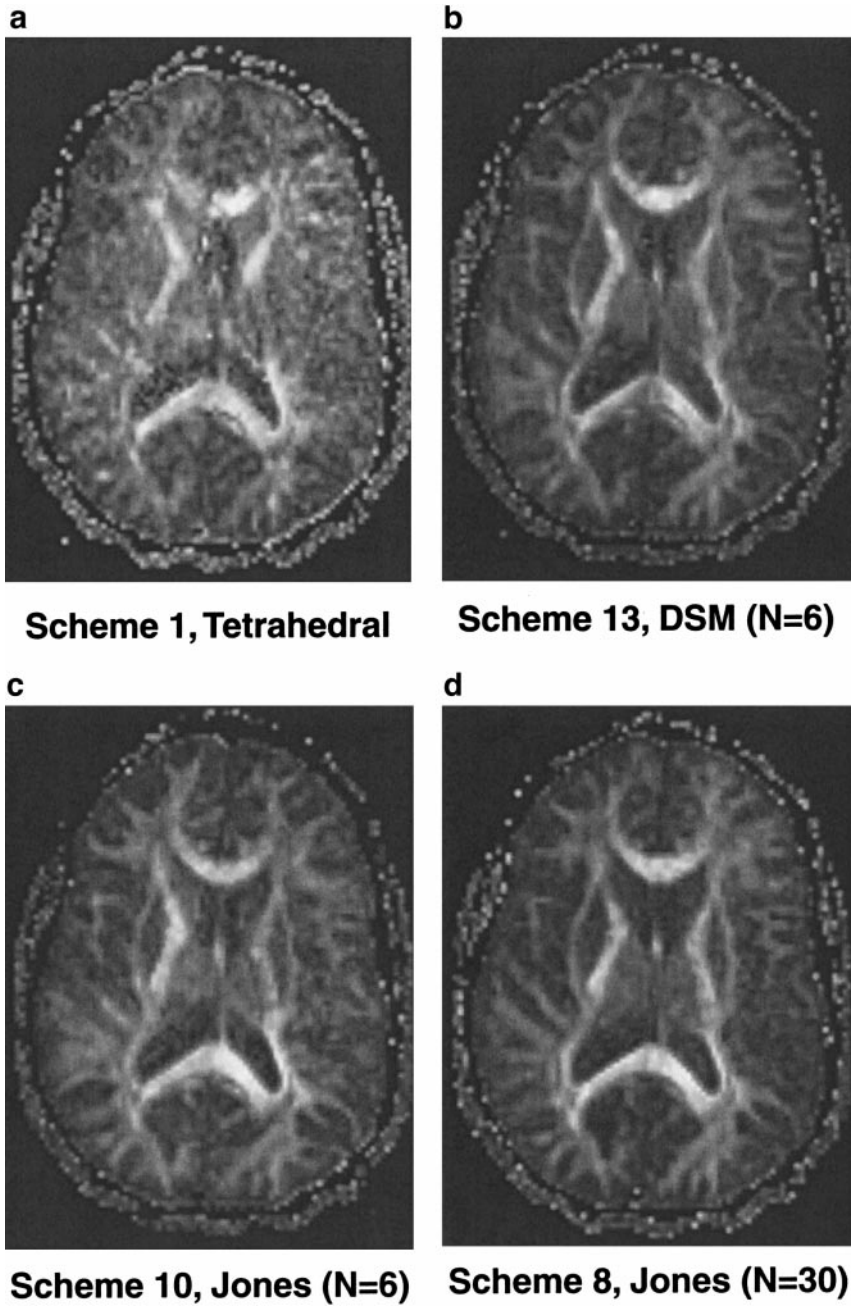

FIG. 6. A representative set of fractional anisotropy maps measured in a normal subject using four different DTI schemes. The results for the tetrahedral (a), DSM (b), Jones6 (c), and Jones30 (d) schemes are shown. The experimental parameters used for MRI measurements were TE = 95 ms, TR = 4 × RR, FOV = 240 mm, and b = 1000 s/mm^2. The spatial resolution was 4 × 1.9 × 1.9 mm. The total number of imaging data acquisitions used for each scheme was about 140 scans.

To our surprise, the DSM schemes were not as robust as the Jones schemes in terms of orientation independence. We attribute this to a tendency in the optimization algorithm to favor the orthogonal axes (x, y, and z) as opposed to a uniform distribution in the entire 3D space, which is a unique feature of the Jones schemes. It is not clear to us why the optimization algorithm favors the orthogonal axes, but this trend is apparent upon visual inspection of the gradient distribution.

In the search for optimal scheme, a low standard deviation and bias in the calculated diffusion tensor are prerequisites for the production of accurate anisotropy maps (*1, 5, 18–22*). For anisotropic diffusion with different diffusion tensor orientations in the same measurement volume, using a single b value for multiple directions is likely to produce ADC maps with regional differences in experimental noise levels (*18*). We have demonstrated this type of noise-induced rotational variance

using simulations of a rice-shaped tensor (Fig. 3). The same conclusion should also hold for other tensor shapes, since Eq. [14] is valid for the general case.

In addition to the condition number, the accuracy of the diffusion tensor measurements is also determined by the noise level of the ADC maps. Due to the presence of different tensor orientations, two DTI schemes with a similar condition number but a different gradient configuration can produce ADC maps with significantly different noise levels if a single optimum *b* value is used. Only when noise levels in ADCs measured in *N* noncollinear direction are identical is the error propagation from ϵ_{ADC} to ϵ_X solely determined by the condition number of the transformation matrix. An effective approach to reduce noise-related rotational variance is to use schemes with uniform and redundant DWI sampling. The use of such a scheme will achieve not only better SNR but also higher contrast between structures with different anisotropy and orientations.

For further investigations in finding the optimum DTI scheme additional constrains may be incorporated into the minimization procedure, such as uniform gradient distribution and simultaneous application of multiple gradients to minimize TE. Further, the algorithm can also be directly applied to σ(FA) instead of the condition number. This might be more computationally intensive but feasible.

CONCLUSION

The condition number of the transformation matrix of a DTI scheme, which determines the sensitivity of error propagations from experimentally measured ADC values to the elements of the diffusion tensor, is an intuitive and objective predictor of the noise performance of the DTI scheme. Results from simulations and MRI measurements are consistent with the theoretical predictions. The minimization of the condition number can be used as a guide to search for new DTI schemes.

For measurements of diffusion tensor with different orientations as in the brain, diffusion-weighted MRI data acquisitions using a single optimum *b* value based on the mean diffusivity can produce an ADC map with regional differences in noise levels. This will give rise to a rotational variance of eigenvalues and anisotropy when diffusion tensor mapping is performed using DTI schemes with limited number of diffusion-weighting gradient directions. To reduce this type of artifact, a DTI scheme with not only a small condition number but also a large number of evenly distributed diffusion-weighting gradients in 3D is the preferred method.

ACKNOWLEDGMENTS

Assistance from Dr. D. K. Jones in providing the software to generate the DTI schemes Jones6–Jones30 is greatly appreciated. M. Hedehus and M. Moseley acknowledge the generous support of the Lucas Foundation as well as NIH Grant 1P41RR09784. T. Q. Li acknowledges support from the Center for the Study of Brain, Mind, and Behavior at Princeton University.

REFERENCES

1. P. J. Basser and C. Pierpaoli, Microstructural and physiological features of tissues elucidated by quantitative-diffusion tensor MRI. *J. Magn. Reson. B* **111,** 209–219 (1996).
2. P. J. Basser, Inferring microstructural features and the physiological state of tissues from diffusion-weighted images, *NMR Biomed.* **8,** 333–344 (1995).
3. P. J. Basser, J. Mattiello, and D. Le Bihan, Estimation of the effective self-diffusion tensor from the NMR spin echo, *J. Magn. Reson. B* **103,** 247–254 (1994).
4. C. Pierpaoli, P. Jezzard, P. J. Basser, A. Barnett, and Di Chiro G, Diffusion tensor MR imaging of the human brain. *Radiology* **201,** 637–648 (1996).
5. C. Pierpaoli and P. J. Basser, Toward a quantitative assessment of diffusion anisotropy, *Magn. Reson. Med.* **36,** 893–906 (1996). [published erratum appears in *Magn. Reson. Med.* **37**(6), 972 (1997)]
6. C. T. Moonen, J. Pekar, M. H. de Vleeschouwer, P. van Gelderen, P. C. van Zijl, and D. DesPres, Restricted and anisotropic displacement of water in healthy cat brain and in stroke studied by NMR diffusion imaging, *Magn. Reson. Med.* **19,** 327–332 (1991).
7. M. S. Buchsbaum, C. Y. Tang, S. Peled, H. Gudbjartsson, D. Lu, E. A. Hazlett, J. Downhill, M. Haznedar, J. H. Fallon, and S. W. Atlas, MRI white matter diffusion anisotropy and PET metabolic rate in schizophrenia. *Neuroreport* **9,** 425–430 (1998).
8. K. O. Lim, M. Hedehus, M. Moseley, A. de Crespigny, E. V. Sullivan, and A. Pfefferbaum, Compromised white matter tract integrity in schizophrenia inferred from diffusion tensor imaging, *Arch. Gen. Psychiatry* **56,** 367–374 (1999).
9. M. Hedehus M, E. V. Sullivann, A. de Crespigny, M. E. Moseley, K. O. Lim, and A. Pfefferbaum, Low white matter anisotropy in chronic alcoholism revealed with diffusion tensor imaging, *in* Abstracts of the International Society of Magnetic Resonance in Medicine, 7th Annual Meeting, Philadelphia, p. 932 (1999).
10. T. Klingberg, M. Hedehus, E. Temple, T. Salz, J. D. E. Gabrieli, M. E. Moseley, and R. A. Poldrack, A neural basis for reading ability: Microstructure of temporo-parietal white matter, *Neuron* **225,** 493–500 (2000).
11. M. A. Horsfield, H. B. Larsson, D. K. Jones, and A. Gass, Diffusion magnetic resonance imaging in multiple sclerosis, *J. Neurol. Neurosurg. Psychiatry* **64**(Suppl. 1), S80–S804 (1998).
12. D. J. Werring, C. A. Clark, G. J. Barker, A. J. Thompso, and D. H. Miller, Diffusion tensor imaging of lesions and normal-appearing white matter in multiple sclerosis, *Neurology* **52,** 1626–1632 (1999).
13. J. J. Neil, S. I. Shiran, R. C. McKinstry, G. L. Schefft, A. Z. Snyder, C. R. Almli, E. Akbudak, J. A. Aronovit, J. P. Miller, B. C. Lee, and T. E. Conturo, Normal brain in human newborns: Apparent diffusion coefficient and diffusion anisotropy measured by using diffusion tensor MR imaging, *Radiology* **209,** 57–66 (1998).
14. T. Klingberg, M. Hedehus, E. Temple, T. Salz, J. D. Gabrieli, M. E. Moseley, and R. A. Poldrack, Myelination and organization of the frontal white matter in children: A diffusion tensor MRI study. *Neuroreport* **10,** 2817–2821 (1999).
15. T. E. Conturo, N. F. Lori, T. S. Cull, E. Akbudak, A. Z. Snyder, J. S. Shimony, R. C. McKinstry, H. Burton, and M. E. Raichle, Tracking neuronal fiber pathways in the living human brain, *Proc. Natl. Acad. Sci. USA* **96,** 10422–10427 (1999).
16. R. Xue, P. van Zijl, B. J. Crain, M. Solaiyappan, and S. Mori, In vivo three-dimensional reconstruction of rat brain axonal projections by diffusion tensor imaging, *Magn. Reson. Med.* **42,** 1123–1127 (1999).

17. P. J. Basser, Fiber-tractography via diffusion tensor MRI (DT-MRI), *in* Abstracts of the International Society of Magnetic Resonance in Medicine, 6th Annual Meeting, Sydney, p. 1226 (1998).
18. S. Skare, T. Q. Li, B. Nordell, and M. Ingvar, Noise considerations in the determination of diffusion tensor anisotropy, *Magn. Reson. Imaging* **18,** 659–669 (2000).
19. M. E. Bastin, P. A. Armitag, and I. Marshall, A theoretical study of the effect of experimental noise on the measurement of anisotropy in diffusion imaging. *Magn. Reson. Imaging* **16,** 773–785 (1998).
20. T. E. Conturo, R. C. McKinstry, E. Akbudak, and B. H. Robinson, Encoding of anisotropic diffusion with tetrahedral gradients: A general mathematical diffusion formalism and experimental results, *Magn. Reson. Med.* **35,** 399–412 (1996).
21. K. M. Martin, N. G. Papadakis, C. L. Huang, L. D. Hall, and T. A. Carpenter, Reduction of the sorting bias in the eigenvalues if the diffusion tensor in diffusion-weighted magnetic resonance imaging, *in* Abstracts of the International Society of Magnetic Resonance in Medicine, 7th Annual Meeting, Philadelphia, p. 1785 (1999).
22. P. J. Basser and S. Pajevic, Method to reduce eigenvalue sorting bias in DT-MRI, *in* Abstracts of the Society of Magnetic Resonance in Medicine, 7th Annual Meeting, Philadelphia, p. 1788 (1999).
23. D. K. Jones, M. A. Horsfield, and A. Simmons, An optimal strategy for precise determination of the diffusion tensor, *in* Abstracts of the International Society of Magnetic Resonance in Medicine, 7th Annual Meeting, Philadelphia, p. 1793 (1999).
24. D. K. Jones, M. A. Horsfield, and A. Simmons, Optimal strategies for measuring diffusion in anisotropic systems by magnetic resonance imaging, *Magn. Reson. Med.* **42,** 515–525 (1999).
25. R. Muthupallai, C. A. Holder, A. W. Song, and W. T. Dixon, *in* Abstracts of the International Society of Magnetic Resonance in Medicine, 7th Annual Meeting, Philadelphia, p. 1825 (1999).
26. N. G. Papadakis, D. Xing, C. L. Huang, L. D. Hall, and T. A. Carpenter, A comparative study of acquisition schemes for diffusion tensor imaging using MRI, *J. Magn. Reson.* **137,** 67–82 (1999).
27. S. Skare and B. Nordell, "Decahedral" gradient encoding for increased accuracy in the estimation of diffusion anisotropy, *in* Abstracts of the International Society of Magnetic Resonance in Medicine, 7th Annual Meeting, Philadelphia, p. 322 (1999).
28. D. K. Jones, D. Lythgoe, M. A. Horsfield, A. Simmons, S. C. Williams, and H. S. Markus, Characterization of white matter damage in ischemic leukoaraiosis with diffusion tensor MRI, *Stroke* **30,** 393–397 (1999).
29. S. Skare, M. Hedehus, and T. Q. Li, Characteristics and stability of different diffusion gradient schemes, *in* Abstracts of the International Society of Magnetic Resonance in Medicine, 8th Annual Meeting, Denver, p. 806 (2000).
30. T. L. Davis, V. J. Wedeen, R. M. Weisskoff, and B. R. Rosen, White Matter Tract Visualization by Echo-Planar MRI, *in* Abstracts of the International Society of Magnetic Resonance in Medicine, 3rd Annual Meeting, New York, p. 289 (1993).
31. P. Pierpaoli, P. Jezzard, P. J. Basser, A. Barnett, and G. di Chiro, Diffusion tensor MR imaging of the human brain, *Radiology* **201**(3), 637–648 (1996).
32. J. A. Nelder and R. Mead, Downhill simplex method for multidimensional minimization, *Comput. J.* **7,** 308–314 (1965).
33. E. O. Stejskal and J. E. Tanner, Spin diffusion measurements: spin echoes in the presence of time-dependent field gradient, *J. Phys. Chem.* **42,** 288–292 (1965).
34. M. Eis and M. Hoehn-Berlage, Correction of gradient cross-talk and optimization of measurement parameters in diffusion MR imaging, *J. Magn. Reson. B* **107,** 222–234 (1995).
35. D. Xing, N. G. Papadakis, C. L.-H. Huang, V. M. Lee, T. A. Carpenter, and L. D. Hall, Optimised diffusion-weighting for measurement of apparent diffusion coefficient (ADC) in human brain, *Magn. Reson. Imaging* **15,** 771–784 (1997).
36. T. E. Tonturo, R. C. McKinstry, A. A. Aronovitz, and J. J. Neil, Diffusion MRI: Precision, accuracy and flow Effects. *NMR Biomed.* **8,** 307–332 (1995).
37. R. M. Henelman, Measurements of signal intensities in the presences of noise in MR images. *Med. Phys.* **12,** 232–241 (1985).
38. S. J. Leon, "Linear Algebra with Applications," 2nd ed. Macmillan, New York, 1986.
39. H. P. William, P. F. Brian, A. T. Saul, and T. V. William, "Numerical Recipes in C," 2nd ed., Cambridge Univ. Press, Cambridge, 1995.
40. A. M. Ulug, N. Beauchamp, R. N. Bryan, and P. C. M. van Zilj, Absolute quantitation of diffusion constants in human stroke, *Stroke* **28,** 483–490 (1997).
41. T. Q. Li, A. Takahashi, T. Hindmarsh, and M. E. Moseley, ADC mapping by means of one-shot spiral MRI technique and preliminary experience in acute cerebral ischemia, *Magn. Reson. Med.* **41,** 141–147 (1999).
42. A. J. de Crespigny and M. E. Moseley, Eddy current induced image warping in diffusion weighted EPI, *in* Abstracts of the International Society of Magnetic Resonance in Medicine, 6th Annual Meeting, Sydney p. 661 (1998).